Faraday Discussions

Cite this: *Faraday Discuss.*, 2024, **251**, 361

PAPER

Dissociative chemisorption of O_2 on Al(111): dynamics on a potential energy surface computed with a non-self-consistent screened hybrid density functional approach†

Robert A. B. van Bree, * Nick Gerrits and Geert-Jan Kroes *

Received 11th December 2023, Accepted 22nd January 2024
DOI: 10.1039/d3fd00165b

Density functional theory (DFT) at the generalized gradient approximation (GGA) level is often considered the best compromise between feasibility and accuracy for reactions of molecules on metal surfaces. Recent work, however, strongly suggests that density functionals (DFs) based on GGA exchange are not able to describe molecule–metal surface reactions for which the work function of the metal surface minus the electron affinity of the molecule is less than 7 eV. Systems for which this is true exhibit an increased charge transfer from the metal to the molecule at the transition state, increasing the delocalisation of the electron density. This enlarged delocalisation can cause GGA-DFT to underestimate energy values relative to the gas-phase and thus underestimate the barrier height, similar to what has been observed for several gas-phase reactions. An example of such a molecule–metal surface system is O_2 + Al(111). Following a similar strategy as for gas-phase reactions, previous work showed results of increased accuracy when using a screened hybrid DF for O_2 + Al(111). However, even screened hybrid DFs are computationally expensive to use for metal surfaces. To resolve this, we test a non-self-consistent field (NSCF) screened hybrid DF approach. This approach computes screened hybrid DFT energies based on self-consistent-field (SCF) GGA electronic densities. Here, we explore the accuracy of the NSCF screened hybrid DF approach by implementing the NSCF HSE03-1/3x@RPBE DF for O_2 + Al(111). We compute and analyse molecular beam sticking probabilities as well as a set of sticking probabilities for rotationally aligned O_2. Our results show that the NSCF approach results in reaction probability curves that reproduce SCF results with near-chemical accuracy, suggesting that the NSCF approach can be used advantageously for exploratory purposes. An analysis of the potential energy surface and the barriers gives insight into the cause of the disagreement between the SCF and NSCF reaction probabilities and into the changes needed in theoretical modelling to further improve

Leiden Institute of Chemisty, Leiden University, Gorlaeus Labaratories, P.O. Box 9502 2300 RA, Leiden, The Netherlands. E-mail: g.j.kroes@chem.leidenuniv.nl

† Electronic supplementary information (ESI) available. See DOI: https://doi.org/10.1039/d3fd00165b

the description of the O_2 + Al(111) system. Finally, the hole model yields fair agreement with dynamics results for the reaction probability curve, but results in an increased slope of the reaction probability curve compared to the molecular dynamics, with a shift to lower or higher energies depending on whether the vibrational energy of the molecule is included in the initial energy of the molecule or not.

Introduction

The dissociative chemisorption (DC) of a molecule reacting on a surface is often considered the rate-controlling step in heterogeneously catalysed processes,[1–3] for instance in ammonia production,[4,5] and steam reforming.[6,7] Moreover, the DC of an O_2 molecule is the initial and often the rate-determining step in oxide formation, corrosion, and catalytic oxidation reactions.[8–12] Understanding the elemental steps at play in the DC of O_2, or other diatomic molecules, is thus of great practical importance. In addition, there is also an intrinsic scientific interest in understanding the breaking and formation of chemical bonds at surfaces.[5,13–16] In the literature, the H_2-on-Cu(111) system is often mentioned as the benchmark system for H_2 dissociation.[15,17–19] Similarly, O_2 on Al has over the years become the benchmark system for the oxidation of metals.[8,20–25] However, theoretical work on the DC of O_2 on Al(111) has thus far not been able to come to an overall consensus on the barrier height for dissociation, the origin of the barrier, and even the reaction mechanism at play.[26–33]

The foremost reason for the disagreement in the theoretical community is that density functionals (DFs) at the generalised gradient approximation (GGA) level of density functional theory (DFT) fail to yield even a qualitatively correct description of the O_2 + Al(111) reaction. The workhorse GGA DF for modelling gas–metal interactions,[16] the PBE[34] DF, fails to predict any barriers for the DC of O_2 on Al(111).[35–37] Moreover, even one of the most repulsive (and therefore 'least reactive') DFs that can be used for molecule–metal systems at the GGA DFT level, the RPBE functional,[38] fails to predict any significant barrier for the dissociation of O_2 on Al(111).[35–37] GGA-level functionals generally incorrectly predict unit reaction probabilities for all incidence energies, *i.e.*, GGA DFs predict a non-activated reaction.[39] This is in contrast with experimental evidence, which shows the DC of O_2 on Al(111) to be an activated reaction.[22] Going beyond semi-local (GGA) functionals to resolve this (or for gas–metal systems in general) is still challenging, as computational costs increase quickly and the dual nature of the system, *i.e.*, the presence of both a molecule and metal surface, makes the choice of functional more difficult. As such, a solution to the theoretical description of the O_2-on-Al(111) system is not readily found.

The failure of GGA-DFT to describe the barrier of O_2 dissociation on Al(111) has, over the years, been attributed to different origins. Behler *et al.*[29,40] argued that the reaction should proceed in an almost diabatic fashion, with spin–orbit coupling only being strong enough to quench the triplet spin of the oncoming O_2 molecule once the barrier on the corresponding 'triplet potential energy surface' has already been passed. They argued that in GGA or other adiabatic DFT approaches, this quenching (which is forbidden in the absence of spin–orbit coupling) incorrectly happens continuously, already occurring for O_2 that is still far from the surface. This should then be why the sticking probability should be

overestimated at the adiabatic RPBE-GGA level of theory, as found in ref. 29. Using an RPBE-DFT approach for computing the potential energy surface (PES) in which the spin state on O_2 was locally constrained to the triplet ground state, they obtained semi-quantitative agreement with sticking experiments in classical molecular dynamics (MD) calculations.[29,40] Carbogno *et al.*[32,33] later made predictions for experiments on the scattering of singlet O_2 from Al(111) that can be used to verify the proposed mechanism, but these experiments have not yet been carried out.

Later, Carter and co-workers argued that the barrier for dissociation of O_2 on Al(111) does not find its origin in spin selection rules but in the occurrence of charge transfer.[26] As Carter and co-workers showed, they were able to compute rather accurate DC barriers for O_2 + Al(111) using an adiabatic approach[26–28] employing an embedded correlated wave function (ECW) method.[41] In these calculations, a second-order multi-reference perturbation theory method, *i.e.*, CASPT2,[42,43] was used to model the interaction of O_2 with an embedded Al cluster. Carter and co-workers attributed[26] the errors in approaches based on GGA DFs to the lack of derivative discontinuities[44] and the self-interaction error.[45] Dynamics calculations based on an embedded CASPT2 PES were in semi-quantitative agreement with sticking experiments,[28] thereby showing that modelling non-adiabatic effects associated with spin–orbit coupling may not be necessary. A disadvantage of their method is that CASPT2 calculations are rather expensive computationally, with the cost scaling as $O(N^5)$ where N is a measure of the size of the system.[46] Perhaps due to high computational costs, the PES was fitted using a minimum of data points, and as a result, a fitting method with limited accuracy (the flexible periodic London–Eyring–Polanyi–Sato, FPLEPS,[47–49] method) had to be used. Furthermore, this unfavourable scaling has possibly stood in the way of achieving further progress using this method for molecules interacting with transition-metal surfaces,[50,51] though recent calculations on H_2 + Cu(111) show much better results with the embedded NEVPT2 method.[52]

One method to correct for the self-interaction error, at least approximately, is to mix exact non-local exchange with semi-local exchange to obtain a hybrid DF. This approach has been used successfully to obtain DFs that are more accurate for gas-phase reaction barriers.[53,54] This idea was further supported by preliminary hybrid DFT calculations on O_2 + Al(111), showing that barriers for dissociation do occur when employing (screened) hybrid functionals to calculate the electronic structure.[24] The suggestion to go beyond the use of semi-local functionals for O_2 + Al(111) also comes from recent work suggesting a correlation of the failure of GGA-DFs for DC on metal surfaces with the so-called charge transfer energy of the system (E_{CT}). This energy may be defined as:[39]

$$E_{CT} = \varphi - EA \quad (1)$$

Here, φ is the work function of the metal surface, and EA is the electron affinity of the molecule. Gerrits *et al.* estimated[39] that the divide between GGA DF failure and success can be found at about 7 eV, *i.e.*, if the charge transfer energy of a system is below 7 eV, charge transfer from the metal to the molecule is more likely and an error in the semi-local GGA-DF is expected to occur and lead to underestimated barrier heights.[39] At 3.76 eV, the charge transfer energy of the O_2-on-Al(111) system is far below 7 eV,[39] and from previous work,[35,36] it is clear that a manner

of delocalization of the O_2 orbitals occurs at the Al surface, which has been pointed to as a cause for underestimating the barrier heights.[55–57] However, we do note that the work of ref. 39 suggests that errors in the density are not necessarily the major cause of the underestimation of the barrier heights, as will be discussed further below.

The above-described correlation of the charge transfer energy of the system with the likely success of GGA functionals, the above-mentioned 'fix' for gas-phase reactions, and preliminary results for O_2 interacting with Al clusters[28] led to dynamics calculations using a screened hybrid DFT PES for O_2 + Al(111).[39] Hybrid DFT has a more favourable computational scaling with system size (as $O(N^4)$)[58] than CASPT2. A screened hybrid functional was used, as global hybrid DFs have severe shortcomings for metals, *e.g.*, their use leads to an underestimated density of states at the Fermi level.[59] The screened hybrid functional dynamics calculations achieved semi-quantitative agreement with experimental sticking coefficients for O_2 + Al(111).[39]

The solution presented in ref. 39 is promising; nevertheless, the use of screened hybrid functionals for gas–metal systems (even for simple metals like Al) is computationally expensive. Nonetheless, if the error of the GGA functional would be mostly functional-driven[60] as opposed to density-driven,[39,60] the electron densities (and Kohn–Sham wavefunction) found from converged GGA DFT calculations might remain accurate. Consequently, using the GGA-DF electron density (and Kohn–Sham wavefunction) to non-self-consistently compute the energy with a screened hybrid functional might represent a viable (*i.e.*, affordable) approach to systems with low electron transfer energies, like O_2 + Al(111). This would enable us to avoid the majority of the computationally expensive cycles with the screened hybrid functional that would be required for self-consistency, and instead achieve results of (near) screened hybrid-level accuracy at only a fraction of the cost. Ref. 39 already suggested that this approach might be viable, by showing, for a limited number of configurations, that a non-self-consistent field (NSCF) hybrid calculation can indeed closely reproduce the self-consistent hybrid barrier heights.[39,61] This finding suggests that the GGA error in the barrier heights for O_2 + Al(111) must be largely functional driven.

In this paper, we explore the potential of the NSCF-screened hybrid functional approach by constructing and analysing an NSCF screened hybrid potential energy surface (PES) for O_2 on Al(111) and using it in dynamics calculations. The resulting NSCF sticking probabilities are compared with SCF results and with results of supersonic beam experiments on sticking of ordinary and rotationally aligned beams. We will show that the NSCF approach reproduces SCF results to within 2 kcal mol^{-1}. The NSCF results are unintentionally in even better agreement with experiments than the SCF results. Furthermore, an analysis of the PES and the reaction barriers, and an analysis using the hole model of Holloway and Nørskov and co-workers[62] give insight into the cause of the disagreement between SCF and NSCF reaction probabilities. Our analysis also shows what type of additions in the theoretical modelling of this challenging benchmark system may be required in future work to improve upon the agreement presently achieved for O_2 + Al(111).

This paper is set up as follows. The next section shortly presents an overview of the methods employed in this work. A more detailed overview of all the methods can be found in the ESI.† Thereafter, the results and discussion section presents

the results in several sub-sections. The first sub-section discusses the importance of a strict convergence of the self-consistent calculations producing the GGA densities. The next two sub-sections present and discuss the results of the dynamics calculations using the NSCF PES for sticking of ordinary and rotationally aligned O_2 in supersonic beams, also comparing them to SCF and experimental results. After this, we discuss the role of the energetic corrugation of the barrier height in the sub-sections. Finally, the last sub-section discusses results for O_2 + Al(111) that are obtained with the hole model.

Methods

In this work, probabilities of dissociative chemisorption of O_2 on Al(111) are computed using the Born–Oppenheimer static surface (BOSS) approximation. Herein, the electronic structure of the system is treated separately from the motion of the nuclei. Likewise, the Al(111) surface atoms are kept fixed in their ideal lattice positions, reducing the dimensionality of the O_2 + Al(111) system to the six degrees of freedom of O_2 (see Section S1.1 of the ESI†).

The electronic energy of O_2 + Al(111) is computed on a grid of points with DFT using the NSCF HSE03-1/3x@RPBE DF; see Section S1.2† for details. All DFT calculations are performed with the Vienna *Ab initio* Simulation Package (VASP) version 5.4.4.[63–67] The initial SCF GGA spin-polarized DFT calculations are carried out with the RPBE[38] functional. The calculations use a 2×2 Al(111) supercell with 4 layers and a vacuum distance of 10 Å. The Al surface is described by a lattice constant of 4.022 Å and interlayer distances of $d_{12} = 2.356$ Å, $d_{23} = 2.248$ Å, and $d_{34} = 2.353$ Å, which are the same as the values used in ref. 39 for the SCF HSE03-1/3x DF calculations. A plane-wave cut-off energy of 400 eV and an $8 \times 8 \times 1$ Γ-centred k-point grid is used. The core electrons are represented *via* the projector augmented wave (PAW)[68] method, and first-order Methfessel–Paxton smearing with a width of 0.2 eV is employed to improve convergence. The energy convergence criterion for the RPBE functional is set to 1×10^{-9} eV. This stringent convergence criterion is specifically chosen with the erratum[61] on the work of ref. 39 in mind and is further discussed in the Results and discussion section.

To complete a NSCF HSE03-1/3x@RPBE calculation, we perform another single-point calculation by applying the HSE03-1/3x DF one time to the pre-converged RPBE density. This calculation uses mostly the same DFT settings as the SCF GGA single-point calculations. The notable difference, however, is the use of the screened hybrid HSE03 (ref. 69) functional with an exact exchange fraction of 1/3. In this calculation, the SCF-RPBE density and Kohn–Sham wavefunction of the previous calculation is used, and the HSE03-1/3x is not applied in a self-consistent manner, but only once to compute the screened hybrid energy from the converged RPBE density.

From the resulting DFT energy grid, a continuous PES is obtained using the corrugation-reducing procedure (CRP),[70,71] which is an interpolation method. The CRP in this work is implemented along the same lines as in ref. 72, with two major distinctions that are discussed in detail in Section S1.3.† Past work indicates that off the DFT data grid, overall, the interpolation error is generally smaller than 2.9 kJ mol^{-1}.[71,73] Additionally, if the molecule–metal interaction energy is smaller than 4 eV, the root mean squared error (RMSE) in the CRP interpolation will normally be less than 0.8 kJ mol^{-1} (ref. 74) (see Section S1.3†). The latter result is

consistent with the small interpolation errors we find in reaction barriers obtained with reduced dimensionality (see Table S2 in the ESI,† which compares reaction-barrier energies directly computed using DFT with CRP values).

Finally, the CRP-PES is used to compute the probabilities of reaction of O_2 on Al(111) *via* dynamics calculations using the quasi-classical trajectory (QCT)[47,75] method. The QCT method incorporates the initial zero-point-vibrational energy of the molecule and uses classical dynamics to propagate the molecular trajectory though time.[39,74,76] Most importantly, incident molecules are started off at 5.0 Å from the surface, with appropriate choice of the molecule's other coordinates and velocities according to the experimental conditions. Trajectories are counted as reacted if the O–O distance becomes larger than 1.59 Å, and as scattered back to the gas phase if the molecule–surface distance becomes larger than 5.0 Å, with the molecule's velocity pointing towards the gas phase. Other implementation details are presented ESI Section S1.4.†

Results and discussion

Converging a non-self-consistent field DFT calculation

As discussed in the Methods section and ESI Section S1.2,† it is important to achieve a high convergence of the DFT energy in the lower-rung calculation of the electron density, to ensure that this density is stable. We found this to be particularly true for geometries in which O_2 is still far away from the Al(111) surface. The NSCF energies can be quite dependent on the convergence of the GGA RPBE density used to evaluate the HSE03-1/3x@RPBE DF. An example of potential problems with less-converged densities is shown in Fig. 1. In this figure, three different cuts through the potential energy surface are shown, plotting the total energy value of O_2 + Al(111) for different bond lengths of O_2 in the gas-phase, *i.e.*, at 5.0 Å above the surface. In Fig. 1A, results obtained with the

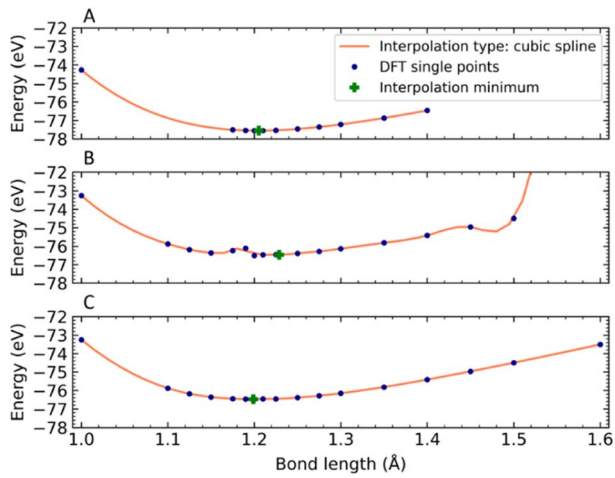

Fig. 1 Three (cubic spline interpolated) potential energy cuts for O_2 at 5 Å above the Al(111) surface, where all degrees of freedom are kept constant except for the oxygen bond length; (A) HSE03-1/3x with an ΔE_{Tol} of 10^{-5} eV; (B) NSCF HSE03-1/3x@RPBE with an RPBE ΔE_{Tol} of 10^{-5} eV; (C) NSCF HSE03-1/3x@RPBE with an RPBE ΔE_{Tol} of 10^{-9} eV.

SCF HSE03-1/3x functional are shown for an energy tolerance $\Delta E_{\mathrm{Tol}} = 10^{-5}$ eV. In Fig. 1B and C, results obtained with the NSCF HSE03-1/3x@RPBE functional are shown for an RPBE tolerance of $\Delta E_{\mathrm{Tol}} = 10^{-5}$ eV in panel B and $\Delta E_{\mathrm{Tol}} = 10^{-9}$ eV in panel C. Fig. 1 clearly shows that obtaining accurate and converged results with the NSCF calculations requires a much lower value of ΔE_{Tol} (a better-converged GGA electron density) than what is needed in an SCF calculation. As also discussed in ESI Section S1.2,† we attribute the NSCF energy's much larger dependence on small changes in the GGA density to the GGA electron density probably not being equal to the electron density that corresponds to the variational minimum for the higher-level functional. In this situation, one would expect to see a much larger dependence of the energy on small variations in the density.

The reaction probability

In Fig. 2, the reaction probability computed with the NSCF hybrid functional (HSE03-1/3x@RPBE) is plotted as a function of incidence energy. We compare these results with reaction probabilities computed with SCF HSE03-1/3x,[39] wave function theory embedded in DFT,[28] RPBE[29,40] and MS-RPBEl (meta-GGA),[39] and with experimental results.[22]

Importantly, the NSCF results reproduce the SCF reaction probabilities within near-chemical accuracy (2 kcal mol^{-1}), but not within chemical accuracy (1 kcal mol^{-1}). The NSCF reaction probabilities appear to be shifted towards somewhat higher incidence energies. This energy shift is not constant: it is larger for higher incidence energies. The increase of the shift also means that the slope of the NSCF reaction probability curve is smaller. This somewhat reduced slope of the NSCF reaction probability curve corresponds to a small broadening of the sticking probability curve relative to the SCF results.

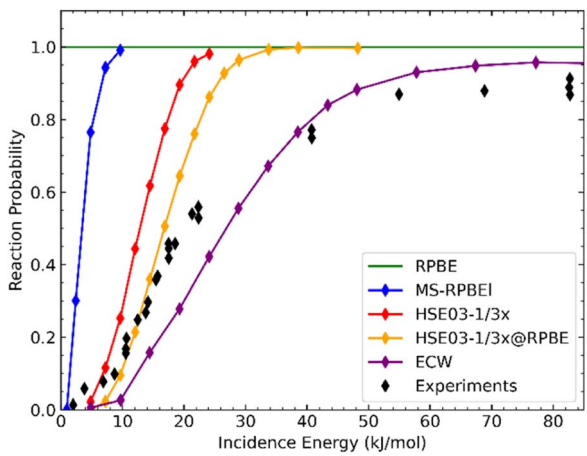

Fig. 2 The reaction probability as a function of incidence energy as computed with the SCF HSE03-1/3x functional (red),[39] the NSCF HSE03-1/3x@RPBE functional (orange) and the embedded correlated wave function method (purple),[28] and as measured in experiments (black),[22] is compared with the reaction probability computed with the RPBE DF (green),[29,40] and with the MS-RPBEl DF (blue).[39]

The difference in incidence energy dependency of the NSCF and SCF HSE03-1/3x sticking curves is visualized in Fig. 3, where we have plotted the incidence energy shift (or Δ) that the SCF HSE03-1/3x reaction probabilities would need to be shifted by to higher energies to morph into the NSCF HSE03-1/3x@RPBE result. At low incidence energy, the energy shift required is small ($\sim$2.4 kJ mol^{-1}) and well within chemical accuracy (1 kcal mol^{-1} $\approx$ 4.2 kJ mol^{-1}), but for larger incidence energies, the required shift increases considerably (to $\sim$7.2 kJ mol^{-1}). Based on the energy shift, we can say that the NSCF results reproduce the SCF results to within chemical accuracy up to an incidence energy of 14 kJ mol^{-1}. The energy shift of the NSCF curve also means that these results reproduce the initial onset of the experimental sticking curve less well (at E_i < 7 kJ mol^{-1}) than the SCF results, but the agreement of the NSCF results with experiments is unintentionally improved in the range of 10–23 kJ mol^{-1}.

The disagreement between the SCF HSE03-1/3x and the NSCF HSE03-1/3x@RPBE results may be surprising when looking back at ref. 39 where (originally) near-exact agreement between SCF and NSCF barriers was reported. Such an agreement would suggest that reaction probability curves would also be in excellent agreement with one another. However, this is, as shown above, not the case. The problem has been resolved, through the recent erratum[61] published on the work of ref. 39, which corrected the reported NSCF 1D potential and further clarified the exact settings used for the published NSCF calculations. It appears that the input parameters in ref. 39 for the SCF RPBE in the NSCF HSE03-1/3x@RPBE functional were set at values not yet sufficiently stringent to obtain a converged NSCF energy. The limited convergence of the GGA density likely resulted in energetic noise in the gas-phase description of the O_2 + Al(111) model (see also Fig. 1). This, in turn, has most likely resulted in incorrect molecule–surface interaction energies, as an unconverged result for O_2 in the gas-phase was subtracted from the energy of the combined system. All in all, this resulted in

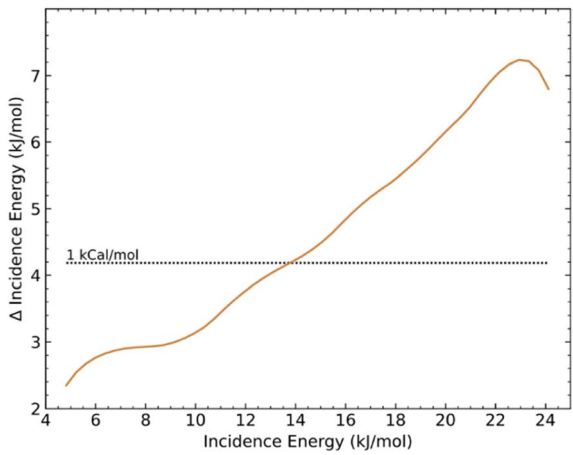

Fig. 3 The amount of incidence energy by which the SCF HSE03-1/3x reaction probability[39] would have to be shifted to morph into the NSCF HSE03-1/3x@RPBE reaction probability curve is shown as a function of the incidence energy of the SCF reaction probability.

a down-shifted barrier height, thereby presenting a too-optimistic picture of the NSCF-screened hybrid DF barrier description.

We found that, when using a plane-wave code like VASP for the O_2-on-Al(111) system, only a small fraction of the computation time for an NSCF hybrid single point is spent on generating a well-converged SCF GGA density. A very stringent convergence setting in the SCF GGA calculation is therefore of little influence on the total computation time. Moreover, the computational cost of an NSCF hybrid single-point calculation is between 1/20th and 1/200th of the cost of a full SCF hybrid single-point calculation. It is, therefore, encouraging to see that the NSCF-screened hybrid results represent a considerable improvement over the RPBE GGA and the MS-RPBEl mGGA results[39] shown in Fig. 2, at a computational cost that is more than an order of magnitude lower than the SCF hybrid DFT calculations. Specifically, we observe that a single application of the screened hybrid functional to a well-converged GGA (*i.e.*, RPBE) density is capable of altering the sticking probability curve to a result much closer to the desired, experimental, outcome and reproduces the SCF hybrid DF with near-chemical accuracy. This last point strengthens the argument made in earlier work[39] that the errors made with GGA functionals when describing systems with a low charge transfer energy, like the O_2 + Al(111) system investigated here, are likely to be mostly functional-driven, with only a small density-driven component.

It would obviously be more elegant if the NSCF results would reproduce the SCF results even more closely so that the HSE03-1/3x@RPBE results could be cast as a very good approximation to the HSE03-1/3x results. In that case, our dynamics calculations would directly test the quality of the DF as used self-consistently, and the comparison with the experiment would be more telling of the quality of the functional itself. The remaining disagreement between SCF and NSCF results does suggest that the DF errors are not entirely functional driven, and that part of the GGA failure is due to errors in the GGA density. This then raises the question of how the density-driven part of the error is related to the system we are treating. Would the disagreement between NSCF and SCF-screened hybrid calculations, where the NSCF calculations are based on GGA densities be smaller if the functionals were applied to systems with smaller charge transfer energies, and would electron densities from mGGA DFs improve the description further? It may be fruitful to explore the answer to these and other related questions, and thereby hopefully learn more about how problems with DFT are related to the type of system to which it is applied, and how such problems may be solved.

Nevertheless, the NSCF-screened hybrid results are in semi-quantitative agreement with experiments and reproduce the SCF results within near-chemical accuracy. This suggests that the NSCF approach could be used in explorative research aimed at extracting reaction barrier heights for difficult dissociative chemisorption on metal systems (*i.e.*, systems that require hybrid DF's for a proper description at great computational costs, with charge transfer energies < 7 eV). This way, hopefully, the best DFs for a given system can be identified in the same fashion as used earlier for 'easy' systems (with charge transfer energies > 7 eV) – see ref. 16 and 51. As discussed there, this would allow minimum reaction barrier heights to be extracted for such systems, as experimental reaction probability curves should only be reproduced if the barriers in the

PES are correctly described (this argument can be based on the hole model,[62] as also discussed in ref. 16).

Sticking of rotationally aligned O_2

In 2013 Kurahashi and Yamauchi showed that the sticking of O_2 on Al(111) depends strongly on the alignment of the O_2 molecule relative to the surface.[25] Using a single spin-rotational state-selected O_2 beam, their work differentiates the sticking between the two different DC mechanisms of O_2 that are at play.[25] Here, the first mechanism is direct DC, which can occur when the molecule is parallel to the surface,[77] *e.g.*, in a helicoptering state. The second mechanism occurs when the molecule is mostly perpendicular to the surface, in which case abstraction can occur.[13,78–81] Kurahashi *et al.* showed that, for lower incidence energies of O_2, only a small fraction of the O_2 reacts through the abstraction mechanism[25] (see also Fig. 4).

Similarly to ref. 39, we simulate the orientationally aligned state-selected O_2 experiments using our NSCF hybrid functional. We ran quasi-classical trajectories for each of the three specific rovibrational states ($v = 0, j = 1$, and $m_j = -1, 0, 1$) and used eqn (1)–(5) from the work of Kurahashi[25] to combine the m_j state-specific reaction probabilities to obtain sticking probabilities for the two orientationally aligned states prepared experimentally. Note that in spectroscopic terms, the rovibrational spin state of O_2 is indicated by $V = 0, J = 2, K = 1$, and $M_K = -1, 0, 1$;[82] the J ought not to be confused with j, which is the angular momentum associated with the rotation of the molecule. The sticking probabilities computed for the two rotationally aligned states with the SCF HSE03-1/3x DF (red),[39] and

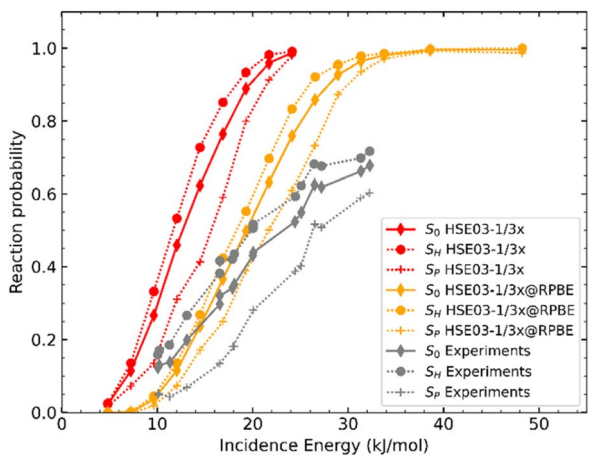

Fig. 4 Total and rotationally resolved sticking curves as a function of incidence energy (kJ mol^{-1}) for molecular beams of O_2 in the $v = 0$, $j = 1$ ($V = 0$, $J = 2$, $K = 1$) state only, as computed with the SCF HSE03-1/3x (red)[39] and NSCF HSE03-1/3x@RPBE (orange) functional, are compared with the measured reaction probabilities (grey).[25] Diamonds and solid lines represent the unaligned state reaction probability (S_0). The circles represent the sticking curves of helicoptering molecules that rotate in a plane parallel to the surface (S_H) and the plus symbols represent the sticking of molecules that are preferentially aligned perpendicular to the surface (S_P).

NSCF HSE03-1/3x@RPBE DF (orange) are compared with those from experiments (grey)[25] in Fig. 4.

The NSCF results for the reaction of rotationally aligned O_2, whether in the helicoptering or the perpendicular state, show a shift of the reaction probability curve towards higher energies relative to the SCF results (Fig. 4), similar to what was observed for the reaction of rotationally unaligned O_2 (Fig. 2). We also observe a slight broadening of the reaction probability curves for both aligned states. However, the qualitative differences between the S_0, S_H, and S_P reaction probabilities are small when comparing the reaction probabilities computed with the SCF and NSCF functionals. The differences in reactivity between the three states, as measured by Kurahashi and Yamauchi[25] and computed by Carter and co-workers,[27,28] are similarly well-described by the NSCF and SCF HSE03-1/3x functionals. These results therefore also point to a functional-driven rather than a density-driven error occurring when GGAs are used to describe the O_2 dissociation on Al(111).

The role of the energetic corrugation of the barrier height

To explain the difference between the NSCF and SCF reaction probabilities, we tabulated the reaction barriers of both DFs, and their difference (Δ) for each elbow cut used to fit the CRP PES in Table 1, and we plotted a sample set of the barrier heights for both approaches (SFC and NSCF) in Fig. 5. This figure (as well as Table 1) shows that all barriers generated using the NSCF approach (orange) are higher in energy than those generated by the SCF approach (red). However, it remains hard to discern a pattern to the shifts in barrier height. There seems to be no constant shift or addition, and the barriers also do not universally scale with a single scalar. There also does not seem to be a clear dependence of the shifts on barrier geometry, nor does the type of surface site seem to influence the shift of the barrier height. However, a consistent trend is that large barriers obtained with the SCF functional correlate with large barriers computed with the NSCF functional and with larger shifts.

The lowest barrier height seen in Table 1 and Fig. 5 (Bridge-P, φ: 0°) corresponds roughly with the sticking curve onset seen in Fig. 2. The minimum SCF barrier height is about 4.7 kJ mol^{-1} and the SCF sticking onset is at approximately the same incidence energy. The NSCF minimum barrier can be found at around 6.6 kJ mol^{-1} and the onset of the NSCF sticking curve is somewhat below 7 kJ mol^{-1}. From these results, it is clear that an incidence energy approximately equal to the minimum barrier height is enough to initialize dissociation for a parallel-oriented O_2 molecule (see also the sub-section: 'Sticking of rotationally aligned O_2'). This is also in agreement with the barriers to dissociation generally being in the entrance channel (see also the potential elbows in Fig. 6 for the barrier locations) of the reaction, with Polanyi's rules[83] dictating that the 10.28 kJ mol^{-1} initial vibrational energy (for the ground state O_2, see also ESI Section S1.4 and Table S1†) is not used to overcome this barrier. As such, for a molecular beam with a rotational temperature of only 9 K (0.03 kJ mol^{-1} for $j = 1$, 80% populated, see Table S1†) the incidence energy should be the only significant component of the molecule's energy that can be used to overcome the barrier.

The barrier height analysis might additionally help with explaining the results of the sticking of rotationally aligned O_2, as the minimum barrier height is found

Table 1 Barrier heights computed with the SCF HSE03-1/3x[39] and NSCF HSE03-1/3x@RPBE DFs, and their difference (Δ) are presented for all elbow cuts used to fit the CRP PES. See Fig. S1B for the name and location of the high symmetry sites; the O_2 orientation is indicated with P (parallel) for $\theta = 90°$, N (normal) for $\theta = 0°$, and T (tilted) for $\theta = 45°$

High symmetry geometry	SCF, HSE03-1/3x Barrier height[39] (kJ mol^{-1})	NSCF HSE03-1/3x@RPBE Barrier height (kJ mol^{-1})	Δ barrier height (kJ mol^{-1})
Top N	26.8	29.8	3.0
Top P, φ: 0°	22.7	24.4	1.7
Top P, φ: 30°	22.5	24.4	1.9
Bridge N	19.5	25.5	6.0
Bridge P, φ: 0°	4.7	6.6	1.8
Bridge P, φ: 60°	19.6	29.7	10.1
Bridge P, φ: 90°	29.5	51.4	21.8
TtF N	22.9	29.1	6.2
TtF T, φ: 150°	26.0	38.0	11.9
TtF T, φ: 240°	12.5	16.7	4.1
TtF T, φ: 330°	14.4	16.6	2.2
TtF P, φ: 240°	23.6	28.7	5.1
TtF P, φ: 330°	10.7	12.8	2.1
TtH N	21.9	27.7	5.8
TtH T, φ: 30°	14.4	16.8	2.4
TtH T, φ: 120°	12.8	16.9	4.1
TtH T, φ: 210°	25.3	36.3	11.1
TtH P, φ: 30°	10.1	12.3	2.2
TtH P, φ: 120°	23.7	37.8	14.1
FCC N	26.9	38.5	11.6
FCC T, φ: 150°	24.6	32.5	7.9
FCC T, φ: 330°	39.9	60.0	20.1
FCC P, φ: 0°	11.5	13.5	2.0
FCC P, φ: 330°	12.4	14.6	2.2
HCP N	22.8	34.6	11.9
HCP T, φ: 210°	23.3	31.0	7.7
HCP T, φ: 30°	39.9	56.2	16.3
HCP P, φ: 0°	10.4	12.7	2.3
HCP P, φ: 30°	11.4	13.7	2.3

for the parallel orientation above a bridge site, and barriers for the reaction with O_2 normal to the surface are found at several kJ mol^{-1} higher energy. It is therefore not surprising that in the limit of low incidence energy, the direct DC mechanism, in which the molecule is parallel to the surface, is favoured.

The analysis of the barrier heights explains why the widths of the sticking probability curves differ for the NSCF and the SCF results. The energetic corrugation of the barrier height is increased with the NSCF approach over the SCF approach, because, as observed in Fig. 5 and Table 1, higher barriers in the SCF approach are correlated with larger positive energy shifts of the NSCF barrier heights relative to the SCF barrier heights. As a result, the difference between the

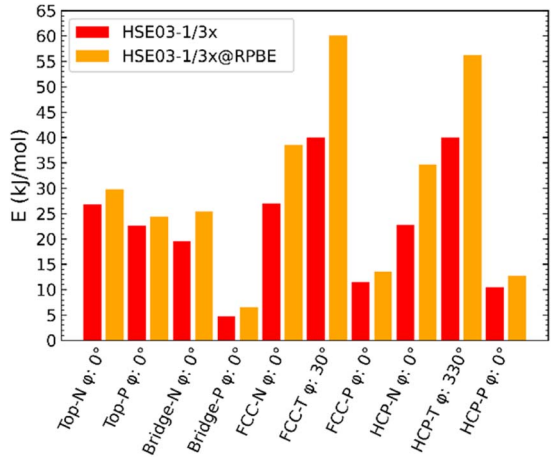

Fig. 5 The barrier heights (in kJ mol^{-1}) calculated with the SCF HSE03-1/3x (red) and the NSCF (orange) HSE03-1/3x@RPBE functional are shown for a large set of different geometries. See Fig. S1B† for the name and location of the high-symmetry sites. The O_2 orientation is indicated with P (parallel) for $\theta = 90°$, N (normal) for $\theta = 0°$, and T (tilted) for $\theta = 45°$.

minimum and maximum barrier heights for HSE03-1/3x@RPBE in Table 1 is much larger (53.5 kJ mol^{-1}) than the analogous difference for the self-consistent HSE03-1/3x DF (35.2 kJ mol^{-1}); see also the underlined barrier heights in Table 1. The higher energetic corrugation of the barriers in the NSCF approach is likely the cause of the increased width (*i.e.*, reduced slope) of the NSCF sticking curve relative to that of the SCF curve, as observed in Fig. 2.[62]

The rather small change of the QCT reaction probability curve width despite the substantial increase of the barrier corrugation (obtained with the NSCF potential) raises concerns about a suggestion made in earlier work.[39] Increasing the energetic corrugation of the barrier height and increasing the anisotropic dependency of the barriers by adding in the attractive van der Waals interaction has been suggested as a way to resolve the difference in slope between the sticking probability curve computed with the HSE03-1/3x functional and the experimental curve.[39] However, with our NSCF approach, we have already inadvertently but considerably changed the barrier corrugation and anisotropy and this is seen to lead only to a minor increase in the width of the sticking curve. Yet, it is unclear what effects van der Waals correlation would have on the dynamics of the reaction. For future theoretical work of O_2 on Al(111), it may still be relevant to not only attempt to increase the energy corrugation or affect the dynamics with the addition of van der Waals correlation, but also to look more closely at non-adiabatic effects that may occur in this system, which may also affect the slope of the sticking curve: systems in which charge transfer is likely, like O_2 on Al(111), may also be more prone to electron–hole-pair excitation.[39,84–86] Additionally, it is not yet known whether or not the thermal displacement of the surface atoms could influence the reaction barriers or whether the sudden approximation will hold for O_2 on Al(111).[18,87,88] Therefore, we might also need to study the effect of thermal displacements of the surface atoms and of energy transfer to surface

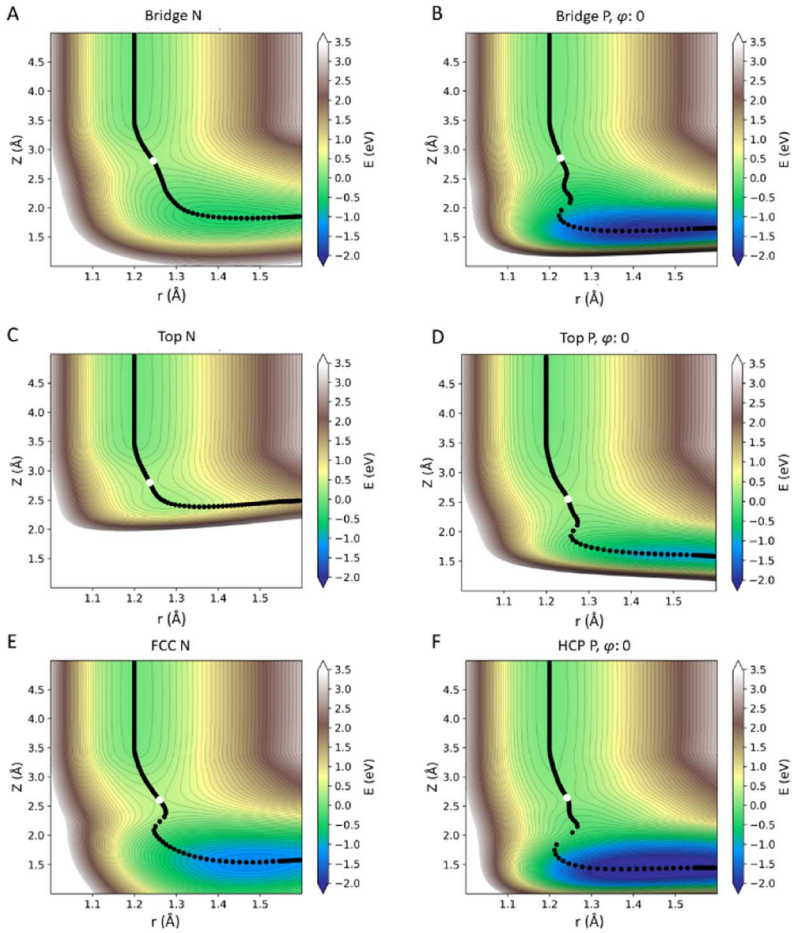

Fig. 6 Set of 6 'elbow cuts', showing slices through the PES as a function of the molecule's bond length (r) and the distance of O_2 to the surface (Z) for six different geometries (sampling four different surface sites and two different molecular orientations). Contour lines are separated by 2 kcal mol^{-1}. Each elbow shows the approximate minimum energy path with black dots. The white dots show the location of the transition state in reduced dimensionality; (A) Bridge N, (B) Bridge P-φ: 0°, (C) Top N, (D) Top P-φ: 0, (E) FCC N, (F) HCP P-φ: 0°.

atom motion. Conversely, experiments show little influence of the surface temperature on the reaction probability,[22] indicating a limited influence of surface motion. However, this has not yet been checked with theory, nor do we know whether the reaction probability can be diminished by energy dissipation to the surface atoms at higher incidence energies. Further theoretical work should address these points.

Although the change in the barrier corrugation appears to be considerable, as stated before, the change of the slope (or width) of the reaction probability curve in Fig. 3 is rather small. This could also suggest that dynamical effects, such as steering, play an active role in the reaction, as was also previously suggested by Carter and co-workers.[27,28] Steering effects have also been indicated in other DC

systems of slowly rotating molecules incident on a surface at low translational energies.[89–92] The importance of steering effects can be investigated with the hole model, as will now be discussed.

The hole model

An interesting way to test for the importance of dynamical effects is by applying the hole model.[62] Put simply, the hole model states that for a particular geometry, a reaction will occur if the translational plus internal energy of the molecule is equal to or greater than the barrier height.[16] Using the hole model, the reaction probability can be approximated in the following way:

$$S_0(E_{\mathrm{mol}}) = \int H\{E_{\mathrm{mol}} - E_{\mathrm{b}}(X,\ Y,\ \theta,\ \varphi)\}\mathrm{d}X\mathrm{d}Y\, d\cos(\theta)\mathrm{d}\varphi \qquad (2)$$

where $H(x)$ is a Heaviside or step function around $x = 0$, and E_{mol} is the total energy of the molecule and is dependent on the incidence energy and molecular internal energy distribution of the nozzle temperature ($T_{\mathrm{N}} = 300$ K) O_2 molecular beam. In eqn (2) X and Y define the projection of the molecule's centre-of-mass on the surface, θ and φ the polar and azimuthal angles of orientation of the molecule with respect to the surface, and E_{b} the barrier height for a particular configuration defined by X, Y, θ, and φ. The method does not include any dynamical effects, but it does include the effect of the distribution of the initial rovibrational O_2 states through its dependence on the initial energy of the molecule. It also includes the effects of the minimum barrier height, the corrugation of the barrier, and the anisotropy of the barrier. The Monte-Carlo-like implementation of the hole model we use is described in detail in Section S1.5 of the ESI.†

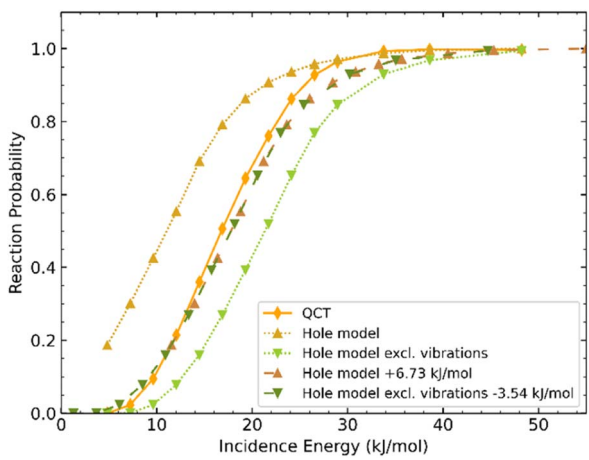

Fig. 7 Reaction probability as a function of incidence energy for the HSE03-1/3x@RPBE DF PES. The results of the QCT method (orange diamonds and solid line), the hole model including vibrational energy (upward-pointing triangles), and the hole model excluding vibrational energy (downward-pointing triangles) are shown. The dashed lines represent shifted reaction probabilities obtained with these versions of the hole model. The shift in incidence energy is 6.73 kJ mol^{-1} to the right for the hole model including vibrational energy, and 3.54 kJ mol^{-1} to the left for the hole model excluding vibrational energy.

In Fig. 7, we show four different hole-model reaction probability curves, where each curve is based on 10^6 samples of initial O_2 energies and geometries taken on the HSE03-1/3x@RPBE PES, and compare them to QCT results obtained with the same PES. The uppermost curve implements the regular hole model (*i.e.*, including the initial vibrational energy; gold upward-pointing triangles interpolated by a dotted line), and the lowest curve shows hole-model results where we excluded the vibrational energy of the molecule (light green downward-pointing triangles, dotted line). Lastly, Fig. 7 presents these same reaction probability curves shifted horizontally by 6.73 kJ mol^{-1} and −3.54 kJ mol^{-1}, respectively (darker-colour variants and dashed lines).

The agreement between the regular hole model and the QCT results is reasonable, although it seems that the regular hole model yields a slightly wider reaction probability curve, and systematically overestimates the QCT reaction probability. However, this overestimation is not unexpected. The hole model assumes that all of the internal energy of the molecule is available to overcome the reaction barrier. This includes zero-point energy (ZPE), which cannot all be used to overcome a barrier. Additionally, we know from Polanyi's rules[83] that converting vibrational energy into motion along the reaction path should be inefficient for an early barrier reaction. We therefore also included hole-model results where we excluded the initial vibrational energy from the total energy of O_2, which leads to a reaction probability curve that is shifted to higher energy by about 10 kJ mol^{-1} relative to the regular hole-model curve. This shift is approximately equal to the vibrational energy of O_2 in $v = 0$ (99% of O_2 is in $v = 0$ at $T_N =$ 300 K; see Table S1†). These results, predictably, now underestimate the QCT reaction probability. Excluding all vibrational energy of the molecule is of course a slight overcorrection on Polanyi's rules, as the early barrier is often found at slightly expanded bond lengths (see also Fig. 6). It is also an overcorrection for the ZPE, as the gas-phase ZPE of the O_2 molecule is not the same as, and typically higher than, the ZPE of O_2 at the transition state.

To best evaluate the different hole-model results, we shifted the two different hole-model curves horizontally to match the onset of the QCT curve as well as possible (the lowest value of the regular hole model is at a reaction probability of 0.186, and thus we match the curves in E_i to this value of the reaction probability; ESI Fig. S2 and S3† show a continuous energy shift of the reaction probabilities for the incidence energy range of 5–30 kJ mol^{-1}, similar to Fig. 3). Matching the curves with the QCT results required shifting the regular hole-model curve to higher energies by 6.7 kJ mol^{-1}, and shifting the hole-model curve excluding the effect of the vibration by 3.5 kJ mol^{-1} to lower energies. Based on this, we can say that the amount of vibrational energy used to overcome the barrier is roughly one-third that of the vibrational energy of O_2 in the gas-phase. Interestingly, shifting the hole-model curves like this reveals a small but clear difference between the widths (or slopes) of the reaction probability curves: the hole-model reaction probability curves are broader than the QCT reaction probability curve. This suggests that dynamical effects, possibly related to steering, occur and that these favour the dissociation of O_2 on Al(111) most at the low incidence energies, where there is time for the forces acting on the molecule to steer it to more favourable geometries for reaction. At the same time, this effect appears to be rather small, suggesting that the hole model can be used as a computationally cheaper screening tool to test electronic structure methods for O_2 + Al(111), or more

generally for systems where dynamical effects are limited. The use of the hole model allows for savings in computation time, not only because dynamics calculations can be skipped, but also because the PES is not required beyond the barrier geometries (*i.e.*, in the exit channel).

Conclusions

O_2 + Al(111) is a benchmark system for modelling O_2 dissociation on metal surfaces and oxide formation. Thus far, the theoretical community has not been able to come to a consensus on the fundamental mechanisms at play in the dissociative chemisorption of O_2 on Al(111). One underlying cause is that GGA functionals (the most commonly used functionals in the study of gas–metal surface interactions) are unable to describe barriers of O_2 dissociative chemisorption on metals correctly if the charge transfer energy (φ − EA) is smaller than 7 eV.[39] Recent work[39] suggested that using a screened hybrid DF will yield better results than GGA functionals, even if the screened hybrid DF is applied in an NSCF manner to a GGA electron density. Here we tested this idea for O_2 + Al(111).

Our results show that the NSCF approach to a screened hybrid density functional (DF) (HSE03-1/3x@RPBE) is indeed a major improvement over GGA (RPBE) or even meta-GGA (MS-RPBEl) DFs for describing the dissociative chemisorption of O_2 on Al(111), while also limiting the extra computational cost by at least one order of magnitude compared to fully self-consistent hybrid calculations. The sticking curves generated with the NSCF-DF are within near-chemical accuracy of the SCF-DF results for both full molecular beam simulations and rotationally aligned sticking. Moreover, with the NSCF approach, the quantitative agreement with experiments was inadvertently improved over that obtained with the SCF HSE03-1/3x approach.

The NSCF-screened hybrid DF was not able to exactly reproduce the SCF-screened hybrid functional results. The onset of the NSCF DF reaction probability at low incidence energy is within chemical accuracy of the SCF results. The NSCF approach leads to a slightly reduced slope of the reaction probability curve, resulting in a slightly increased disagreement with the SCF results at larger incidence energies. This can be traced back to the differences in barrier heights between the SCF and NSCF methods. The NSCF barrier heights are shifted to higher energies relative to the SCF barriers by a minimum of 1.8 kJ mol^{-1}, with the difference increasing with the SCF barrier height. Overall the anisotropic variation of the barrier height and the corrugation of the barrier height have been increased by the NSCF approach relative to the SCF HSE03-1/3x DF case. This has resulted in a minor decrease in the slope of the reaction probability curve and, conversely, a slight increase in its width.

Irrespective of the small quantitative disagreement in sticking probabilities and barrier heights obtained with the NSCF and SCF approaches, the argument that originally inspired us to explore the NSCF approach (accurate while being much cheaper computationally) still holds considerable credence based on the results of this work. It is clear that based on only a GGA density, we can achieve vast improvement in the interaction energy of O_2 + Al(111) simply by non-self-consistently applying a screened hybrid functional to a GGA electron density once. Based on the small differences between the SCF and the NSCF results, we conclude that the greater part of the error in describing the O_2 +

Al(111) system with a GGA DF is functional-driven and not density-driven. However, the remaining disagreement between the SCF and NSCF results suggests that a small density-driven error from using a GGA-level functional is still present.

Increasing the width of the sticking curve of O_2 on Al(111) remains a priority for future work, as the onset of the sticking curve is described with good agreement with both the SCF and NSCF functionals. Previous work suggested that this could be achieved by increasing the corrugation and anisotropy of barriers by incorporating van der Waals correlation into the DF. The QCT and hole-model reaction probability comparison suggests that the corrugation and anisotropy of the barrier may, however, not be the only factors influencing the width of the sticking curve. Nonetheless, the effect of including van der Waals correlation in the DF on the dynamics should still be investigated. At the same time, due to the low charge transfer energy, electron–hole-pair excitations may need to be taken into account in future work, which could help to further broaden the sticking curve. Furthermore, introducing surface atom motion could also affect the width of the computed sticking probability curve for O_2 on Al(111), by either influencing the barriers *via* thermal surface atom displacements or through energy transfer between the motions of O_2 and the Al surface atoms.

Author contributions

Conceptualization: N. Gerrits, G. J. Kroes; data curation: R. A. B. van Bree; formal analysis: R. A. B. van Bree; funding acquisition: G. J. Kroes; investigation: R. A. B. van Bree; methodology: R. A. B. van Bree, N. Gerrits, G. J. Kroes; project administration: G. J. Kroes; resources: G. J. Kroes; software: R. A. B. van Bree, N. Gerrits; supervision: G. J. Kroes; validation: R. A. B. van Bree, N. Gerrits, G. J. Kroes; visualization: R. A. B. van Bree; writing – original draft: R. A. B. van Bree; writing – review & editing: R. A. B. van Bree, N. Gerrits, G. J. Kroes.

Conflicts of interest

There are no conflicts to declare.

Acknowledgements

We would like to thank Mark Somers for the extensive assistance with running computations and for maintaining our computational clusters. Moreover, we would like to thank Bauke Smits, Egidius Smeets, Lukas Hückmann, Theophile Tchakoua, Jonathon Cottom, and Stefan Vuckovic for their assistance and insightful discussions.

References

1 G. Ertl, *Angew. Chem., Int. Ed. Engl.*, 1990, **29**, 1219–1227.
2 M. K. Sabbe, M.-F. Reyniers and K. Reuter, *Catal. Sci. Technol.*, 2012, **2**, 2010–2024.
3 C. A. Wolcott, A. J. Medford, F. Studt and C. T. Campbell, *J. Catal.*, 2015, **330**, 197–207.

4 G. Ertl, *J. Vac. Sci. Technol., A*, 1983, **1**, 1247–1253.
5 G. Ertl, *Angew. Chem., Int. Ed.*, 2008, **47**, 3524–3535.
6 K. C. Waugh, *Catal. Today*, 1992, **15**, 51–75.
7 J. R. Rostrup-Nielsen, J. Sehested and J. K. Nørskov, *Adv. Catal.*, 2002, **47**, 65–139.
8 P. O. Gartland, *Surf. Sci.*, 1977, **62**, 183–196.
9 M. W. Roberts, *Chem. Soc. Rev.*, 1989, **18**, 451–475.
10 E. Lundgren, A. Mikkelsen, J. N. Andersen, G. Kresse, M. Schmid and P. Varga, *J. Phys.: Condens. Matter*, 2006, **18**, R481–R499.
11 C. Stampfl, A. Soon, S. Piccinin, H. Shi and H. Zhang, *J. Phys.: Condens. Matter*, 2008, **20**, 184021.
12 M. M. Montemore, M. A. van Spronsen, R. J. Madix and C. M. Friend, *Chem. Rev.*, 2018, **118**, 2816–2862.
13 J. Jacobsen, B. Hammer, K. W. Jacobsen and J. K. No/rskov, *Phys. Rev. B: Condens. Matter Mater. Phys.*, 1995, **52**, 14954–14962.
14 G. R. Darling and S. Holloway, *Rep. Prog. Phys.*, 1995, **58**, 1595–1672.
15 G.-J. Kroes and C. Díaz, *Chem. Soc. Rev.*, 2016, **45**, 3658–3700.
16 G.-J. Kroes, *Phys. Chem. Chem. Phys.*, 2021, **23**, 8962–9048.
17 C. Díaz, E. Pijper, R. A. Olsen, H. F. Busnengo, D. J. Auerbach and G. J. Kroes, *Science*, 2009, **326**, 832–834.
18 M. Wijzenbroek and M. F. Somers, *J. Chem. Phys.*, 2012, **137**, 054703.
19 B. Smits and M. F. Somers, *J. Chem. Phys.*, 2022, **157**, 134704.
20 I. P. Batra and L. Kleinman, *J. Electron Spectrosc. Relat. Phenom.*, 1984, **33**, 175–241.
21 M. Kerkar, D. Fisher, D. P. Woodruff and B. Cowie, *Surf. Sci.*, 1992, **271**, 45–56.
22 L. Österlund, I. Zoric-acute and B. Kasemo, *Phys. Rev. B: Condens. Matter Mater. Phys.*, 1997, **55**, 15452–15455.
23 V. Zhukov, I. Popova and J. T. Yates, *Surf. Sci.*, 1999, **441**, 251–264.
24 H.-R. Liu, H. Xiang and X. G. Gong, *J. Chem. Phys.*, 2011, **135**, 214702.
25 M. Kurahashi and Y. Yamauchi, *Phys. Rev. Lett.*, 2013, **110**, 246102.
26 F. Libisch, C. Huang, P. Liao, M. Pavone and E. A. Carter, *Phys. Rev. Lett.*, 2012, **109**, 198303.
27 J. Cheng, F. Libisch and E. A. Carter, *J. Phys. Chem. Lett.*, 2015, **6**, 1661–1665.
28 R. Yin, Y. Zhang, F. Libisch, E. A. Carter, H. Guo and B. Jiang, *J. Phys. Chem. Lett.*, 2018, **9**, 3271–3277.
29 J. Behler, B. Delley, S. Lorenz, K. Reuter and M. Scheffler, *Phys. Rev. Lett.*, 2005, **94**, 036104.
30 X. L. Fan, W. M. Lau and Z. F. Liu, *Phys. Rev. Lett.*, 2006, **96**, 079801.
31 J. Behler, K. Reuter and M. Scheffler, *Phys. Rev. Lett.*, 2006, **96**, 79802.
32 C. Carbogno, J. Behler, A. Groß and K. Reuter, *Phys. Rev. Lett.*, 2008, **101**, 096104.
33 C. Carbogno, J. Behler, K. Reuter and A. Groß, *Phys. Rev. B: Condens. Matter Mater. Phys.*, 2010, **81**, 035410.
34 J. P. Perdew, K. Burke and M. Ernzerhof, *Phys. Rev. Lett.*, 1996, **77**, 3865–3868.
35 T. Sasaki and T. Ohno, *Phys. Rev. B: Condens. Matter Mater. Phys.*, 1999, **60**, 7824–7827.
36 K. Honkala and K. Laasonen, *Phys. Rev. Lett.*, 2000, **84**, 705–708.
37 Y. Yourdshahyan, B. Razaznejad and B. I. Lundqvist, *Phys. Rev. B: Condens. Matter Mater. Phys.*, 2002, **65**, 075416.

38 B. Hammer, L. B. Hansen and J. K. Nørskov, *Phys. Rev. B: Condens. Matter Mater. Phys.*, 1999, **59**, 7413–7421.
39 N. Gerrits, E. W. F. Smeets, S. Vuckovic, A. D. Powell, K. Doblhoff-Dier and G.-J. Kroes, *J. Phys. Chem. Lett.*, 2020, **11**, 10552–10560.
40 J. Behler, K. Reuter and M. Scheffler, *Phys. Rev. B: Condens. Matter Mater. Phys.*, 2008, **77**, 115421.
41 C. Huang, M. Pavone and E. A. Carter, *J. Chem. Phys.*, 2011, **134**, 154110.
42 K. Andersson, P. A. Malmqvist, B. O. Roos, A. J. Sadlej and K. Wolinski, *J. Phys. Chem.*, 1990, **94**, 5483–5488.
43 K. Andersson, P.-Å. Malmqvist and B. O. Roos, *J. Chem. Phys.*, 1992, **96**, 1218–1226.
44 J. P. Perdew, R. G. Parr, M. Levy and J. L. Balduz, *Phys. Rev. Lett.*, 1982, **49**, 1691–1694.
45 J. P. Perdew and A. Zunger, *Phys. Rev. B: Condens. Matter Mater. Phys.*, 1981, **23**, 5048–5079.
46 F. Menezes, D. Kats and H.-J. Werner, *J. Chem. Phys.*, 2016, **145**, 124115.
47 M. Karplus, R. N. Porter and R. D. Sharma, *J. Chem. Phys.*, 1965, **43**, 3259–3287.
48 J. H. McCreery and G. Wolken, *J. Chem. Phys.*, 1975, **63**, 2340–2349.
49 L. Martin-Gondre, C. Crespos, P. Larrégaray, J. C. Rayez, D. Conte and B. van Ootegem, *Chem. Phys.*, 2010, **367**, 136–147.
50 Q. Zhao, X. Zhang, J. M. P. Martirez and E. A. Carter, *J. Chem. Theory Comput.*, 2020, **16**, 7078–7088.
51 T. Tchakoua, N. Gerrits, E. W. F. Smeets and G.-J. Kroes, *J. Chem. Theory Comput.*, 2023, **19**, 245–270.
52 Z. Wei, J. M. P. Martirez and E. A. Carter, *J. Chem. Phys.*, 2023, **159**, 194108.
53 R. Peverati and D. G. Truhlar, *Philos. Trans. R. Soc., A*, 2014, **372**, 20120476.
54 N. Mardirossian and M. Head-Gordon, *Mol. Phys.*, 2017, **115**, 2315–2372.
55 P. Mori-Sánchez, A. J. Cohen and W. Yang, *J. Chem. Phys.*, 2006, **125**, 201102.
56 P. Mori-Sánchez, A. J. Cohen and W. Yang, *Phys. Rev. Lett.*, 2008, **100**, 146401.
57 A. J. Cohen, P. Mori-Sánchez and W. Yang, *Science*, 2008, **321**, 792–794.
58 J. Zheng, Y. Zhao and D. G. Truhlar, *J. Chem. Theory Comput.*, 2009, **5**, 808–821.
59 W. Gao, T. A. Abtew, T. Cai, Y. Y. Sun, S. Zhang and P. Zhang, *Solid State Commun.*, 2016, **234–235**, 10–13.
60 E. Sim, S. Song and K. Burke, *J. Phys. Chem. Lett.*, 2018, **9**, 6385–6392.
61 N. Gerrits, E. W. F. Smeets, S. Vuckovic, A. D. Powell, K. Doblhoff-Dier and G.-J. Kroes, *J. Phys. Chem. Lett.*, 2022, **13**, 10575–10576.
62 M. Karikorpi, S. Holloway, N. Henriksen and J. K. Nørskov, *Surface Science Letters*, 1987, **179**, L41–L48.
63 G. Kresse and J. Hafner, *Phys. Rev. B: Condens. Matter Mater. Phys.*, 1994, **49**, 14251–14269.
64 G. Kresse and J. Hafner, *J. Phys.: Condens. Matter*, 1994, **6**, 8245–8257.
65 G. Kresse and J. Furthmüller, *Comput. Mater. Sci.*, 1996, **6**, 15–50.
66 G. Kresse and D. Joubert, *Phys. Rev. B: Condens. Matter Mater. Phys.*, 1999, **59**, 1758–1775.
67 G. Kresse and J. Furthmüller, *Phys. Rev.*, 1996, **54**, 11169.
68 P. E. Blöchl, *Phys. Rev. B: Condens. Matter Mater. Phys.*, 1994, **50**, 17953–17979.
69 J. Heyd, G. E. Scuseria and M. Ernzerhof, *J. Chem. Phys.*, 2003, **118**, 8207–8215.
70 H. F. Busnengo, A. Salin and W. Dong, *J. Chem. Phys.*, 2000, **112**, 7641–7651.

71 R. A. Olsen, H. F. Busnengo, A. Salin, M. F. Somers, G. J. Kroes and E. J. Baerends, *J. Chem. Phys.*, 2002, **116**, 3841–3855.
72 M. Wijzenbroek, D. M. Klein, B. Smits, M. F. Somers and G. J. Kroes, *J. Phys. Chem. A*, 2015, **119**, 12146–12158.
73 A. D. Powell, N. Gerrits, T. Tchakoua, M. F. Somers, H. F. Busnengo, J. Meyer, G. Kroes and K. Doblhoff-Dier, *J. Phys. Chem. Lett.*, 2024, **15**, 307–315.
74 E. W. F. Smeets and G. J. Kroes, *J. Phys. Chem. C*, 2021, **125**, 8993–9010.
75 L. M. Raff and M. Karplus, *J. Chem. Phys.*, 1966, **44**, 1212–1229.
76 N. Gerrits, J. Geweke, E. W. F. Smeets, J. Voss, A. M. Wodtke and G.-J. Kroes, *J. Phys. Chem. C*, 2020, **124**, 15944–15960.
77 M. Schmid, G. Leonardelli, R. Tscheließnig, A. Biedermann and P. Varga, *Surf. Sci.*, 2001, **478**, L355–L362.
78 G. Wahnström, A. B. Lee and J. Strömquist, *J. Chem. Phys.*, 1996, **105**, 326–336.
79 M. Binetti, O. Weiße, E. Hasselbrink, A. J. Komrowski and A. C. Kummel, *Faraday Discuss.*, 2000, **117**, 313–320.
80 M. Binetti, O. Weiße, E. Hasselbrink, G. Katz, R. Kosloff and Y. Zeiri, *Chem. Phys. Lett.*, 2003, **373**, 366–371.
81 M. Binetti and E. Hasselbrink, *J. Phys. Chem. B*, 2004, **108**, 14677–14684.
82 M. W. P. Strandberg and M. Tinkham, *Phys. Rev.*, 1955, **97**, 937–966.
83 J. C. Polanyi, *Science*, 1987, **236**, 680–690.
84 G. Füchsel, M. Del Cueto, C. Díaz and G. J. Kroes, *J. Phys. Chem. C*, 2016, **120**, 25760–25779.
85 P. Spiering and J. Meyer, *J. Phys. Chem. Lett.*, 2018, **9**, 1803–1808.
86 P. Spiering, K. Shakouri, J. Behler, G. J. Kroes and J. Meyer, *J. Phys. Chem. Lett.*, 2019, **10**, 2957–2962.
87 A. K. Tiwari, S. Nave and B. Jackson, *Phys. Rev. Lett.*, 2009, **103**, 253201.
88 A. K. Tiwari, S. Nave and B. Jackson, *J. Chem. Phys.*, 2010, **132**, 134702.
89 A. C. Luntz, M. D. Williams and D. S. Bethune, *J. Chem. Phys.*, 1988, **89**, 4381–4395.
90 L. Jacobse, A. den Dunnen and L. B. F. Juurlink, *J. Chem. Phys.*, 2015, **143**, 014703.
91 M. Gostein and G. O. Sitz, *J. Chem. Phys.*, 1997, **106**, 7378–7390.
92 N. Shenvi, S. Roy and J. C. Tully, *Science*, 2009, **326**, 829–832.